COMPUTER RESEARCH AND MODELING
2026 VOL. 18 NO. 2 P. e289–e313
DOI: 10.20537/2076-7633-2026-18-2-289-313

Ки&М

MATHEMATICAL MODELING AND NUMERICAL SIMULATION

UDC: 532.5

On the A. N. Kolmogorov hypotheses-based evaluation of the pulsation spectrum for a time sample of 3D velocity vector components

S. A. Kusyumov, A. N. Kusyumov[a], E. V. Romanova

Kazan National Research Technical University named after A. N. Tupolev,
10 K. Marx st., Kazan, 420111, Russia

E-mail: [a] postbox7@mail.ru

Received 30.09.2025, after completion — 26.12.2025.
Accepted for publication 26.02.2026.

The Fourier transformation is the basic tool for evaluating the spectral characteristics of a turbulent flow. The Fourier transform (usually discrete) of the first power of the longitudinal or transverse component of the velocity vector pulsations allows estimation of the energy spectral density (ESD) or power spectral density (PSD). To estimate the ESD and PSD of a turbulent signal obtained from numerical simulation, an array of signal values with discretization in the time or spatial domain is generated. The reference distribution of the ESD spectrum (scaling law) within the wave number domain of the inertial subrange is derived from two hypotheses proposed by A.N. Kolmogorov and is characterized by the $-\frac{5}{3}$ law. The $-\frac{5}{3}$ law is also used in most references to estimate the ESD distribution in the frequency domain. The distribution of the power spectrum PSD is derived from the distribution of the energy spectrum ESD by normalizing to the signal scanning time. An alternative energy spectral characteristic (ESS) of velocity fluctuations can be determined by the Fourier transform of the square of the velocity fluctuations. In the wave numbers domain, the dimension of ESS in the spatial domain coincides with the dimension of A. N. Kolmogorov's $-\frac{5}{3}$ law. When considering a signal sampled in the time domain, a scaling law of -2 for ESS was previously obtained in the frequency domain. An alternative estimate of the Power Signal Spectrum (PSS) is discussed in this paper based on the Fourier transform of the third-order velocity pulsations. Based on the hypotheses proposed by A. N. Kolmogorov, it can be inferred that in the frequency domain, the scaling law of the PSS spectrum is characterized by the power of $-\frac{5}{2}$. Unsteady incompressible flow around a 3D cylindrical surface section at the Reynolds number of 3900 is considered as an application. The numerical simulation is performed using ANSYS Fluent commercial code and based on the Navier – Stokes equations. The spatio-temporal characteristics of the turbulent flow velocity vector are analyzed using the Proper Orthogonal Decomposition (POD). The Fourier transform is used to estimate the ESS and PSS of a time-sampled signal.

Keywords: Navier – Stokes equations, turbulence, spectrum, Kolmogorow's law, cylinder, proper orthogonal decomposition

Citation: *Computer Research and Modeling*, 2026, vol. 18, no. 2, pp. e289–e313.

КОМПЬЮТЕРНЫЕ ИССЛЕДОВАНИЯ
И МОДЕЛИРОВАНИЕ 2026 Т. 18 № 2 С. e289–e313
DOI: 10.20537/2076-7633-2026-18-2-289-313

Ки&М

МАТЕМАТИЧЕСКИЕ ОСНОВЫ И ЧИСЛЕННЫЕ МЕТОДЫ МОДЕЛИРОВАНИЯ

УДК: 532.5

К оценке спектра пульсаций временной выборки компонент 3D-вектора скорости на основе гипотез А. Н. Колмогорова

С. А. Кусюмов, А. Н. Кусюмов[a], Е. В. Романова

Казанский национальный исследовательский технический университет имени А. Н. Туполева,
Россия, 420111, г. Казань, ул. К. Маркса, д. 10

E-mail: [a] postbox7@mail.ru

Получено 30.09.2025, после доработки — 26.12.2025.
Принято к публикации 26.02.2026.

Преобразование Фурье является основным инструментом для оценки спектральных характеристик турбулентного течения. Применение преобразования Фурье (как правило, дискретного) к первой степени пульсационной продольной или поперечной компоненты вектора скорости позволяет оценить спектральную плотность энергии (ESD) или мощности (PSD). Для оценки ESD и PSD турбулентного сигнала, полученного по результатам численного моделирования обтекания тела, создается массив значений сигнала с дискретизацией во временной или пространственной области. Референтное распределение спектральной характеристики ESD (закон масштабирования) в области волновых чисел инерциального поддиапазона следует из двух гипотез А. Н. Колмогорова и определяется законом $-\frac{5}{3}$. Закон $-\frac{5}{3}$ используется также в большинстве работ для оценки распределения ESD и PSD в частотной области. При этом распределение спектра мощности PSD получается из распределения спектра энергии ESD нормировкой к времени сканирования сигнала. Альтернативная спектральная характеристика энергии (ESS) пульсаций скорости может быть определена преобразованием Фурье для квадрата пульсаций скорости. Размерность ESS в пространственной области совпадает с размерностью закона $-\frac{5}{3}$ А. Н. Колмогорова в области волновых чисел. При дискретизации сигнала во временной области для ESS ранее получен закон масштабирования -2 в частотной области. В настоящей работе вводится альтернативная оценка спектра мощности сигнала (PSS), полученная с использованием преобразования Фурье для третьей степени пульсаций скорости. Из гипотез А. Н. Колмогорова следует, что в частотной области закон масштабирования спектра PSS определяется степенью $-\frac{5}{2}$. В качестве приложения рассматривается нестационарное обтекание отсека цилиндрической 3D-поверхности при числе Рейнольдса 3900. Численное моделирование выполнено с использованием пакета ANSYS Fluent на базе решения уравнений Навье – Стокса в несжимаемой постановке. Пространственно-временные характеристики вектора скорости турбулентного потока анализируются с применением правильной ортогональной декомпозиции (POD). Для оценки ESS и PSS используется преобразование Фурье с дискретизацией сигнала по времени.

Ключевые слова: уравнения Навье – Стокса, турбулентность, спектр, закон Колмогорова, цилиндр, правильная ортогональная декомпозиция

1. Introduction

The flow at some distance from the surface of a bluff body exhibits properties of a turbulent flow, even at quite low values of the Reynolds (Re) number. The flow behind bluff bodies has a significantly three-dimensional character even if the flow is gradient-free along one of the coordinates (for example, for 3D flow with periodic boundary conditions). One of the objectives in the study of turbulent flows is to determine the spectral features of flow parameters. Spectral examination of signal energy, established by the temporal sampling of the velocity vector's components, is a defining element in the majority of investigations pertaining to turbulent flow. A complete description of a turbulent flow, where the flow variables are functions of space and time, can be obtained by numerically solving the Navier – Stokes equations. These numerical solutions are termed the Direct Numerical Simulations (DNS) [Moin, Mahesh, 1998].

To describe the Energy Spectral Density (ESD) of a signal (velocity vector components) under isotropic turbulence conditions, the K41 scaling law $\mathrm{ESD} \sim k^{-5/3}$ is used in the references (k is the wave number) [Kolmogorov, 1991]. Traditionally, the $-\frac{5}{3}$ law is analyzed in relation to the square of the Fourier transform of the fluctuations in the velocity of a turbulent flow. It should be noted that the $-\frac{5}{3}$ law was obtained for the spatial spectrum of the longitudinal and transverse components of the velocity vector. In [Kolmogorov, 1962], it is proposed to determine the statistical performances of turbulence taking into account intermittency in turbulent flows. In this case, the scaling law $-\frac{5}{3}$ for the spatial spectrum of ESD can be represented in a more generalized form: $\mathrm{ESD} \sim k^{-5/3-\mu}$, where $\mu =$ = const (see [Kraichnan, 1974]).

In [Kraichnan, 1974] the value $\mu = 0.05/9$ was considered, which gives a minor change in the scaling $-\frac{5}{3}$ law. In [Long, 2003], based on the analysis of data for a tidal channel flow at high Reynolds numbers, it is argued that the energy spatial spectrum scales with a power of -2 $\left(\mu = \frac{1}{3}\right)$. A similar scaling law was obtained in [Dou, 2022].

In most references modeling the spectrum of the flow velocity vector, the $-\frac{5}{3}$ law is also used to estimate the spectrum of a signal sampled in the temporal domain. The basis for the transition from the spatial to the temporal spectrum is Taylor's hypothesis of "frozen turbulence" [Taylor, 1938]. In [Lathi, Ding, 2010] an approach to ESD analysis in the temporal domain is presented using the first-degree Fourier transform of the turbulent signal (flow velocity fluctuations). In [Tennekies, Lumley, 1972], the statistical theory of turbulence has been utilized to obtain the scaling law ω^{-2} to evaluate the energy spectrum in the temporal domain (ω is the angular frequency). The question of representation of the turbulent signal to determine spectral characteristics remains unresolved in [Tennekies, Lumley, 1972]. It is important to highlight that the study conducted by Tennekies and Lumley did not address the matter of how the turbulent signal is represented (its form) when assessing its spectral characteristics. Later, the scaling law -2 $\left(\omega^{-2}\right)$ was also obtained in [Kusyumov et al., 2023]. To compare spectral characteristics with the -2 law, [Kusyumov et al., 2023] suggested using the Fourier transform for the second power of fluctuations (instantaneous energy) of the longitudinal or transverse components of the flow velocity vector.

Turbulent flow is characterized by a vast range of length scales ranging from the smallest (the Kolmogorov scale) to the largest, determined by the geometry [Pope, 2000] of a simulation domain. The required computer resources and time constraints hinder using the DNS-approach for turbulent flows at high Reynolds numbers. Analysis [Pope, 2000] shows that the number of required grid points for 3D isotropic (in three directions) turbulent flow is proportional to $\mathrm{Re}^{9/4}$.

The engineering computation of turbulent flows therefore relies on approaches based on the Unsteady Reynolds – averaged Navier – Stokes (URANS) equations. Another approximation, the Large

Eddy Simulation (LES), is a compromise in the complexity approach between the DNS and URANS (see reviews [Lesieur, Metais, 1996; Moin, 1997]).

The LES-approach uses spatial averaging instead of temporal averaging. The main goal of LES is to determine equations for the "average speed" whose spectrum does not contain high frequencies. The LES equations are only applicable to scales that exceed a given positive averaging radius. LES-methods were introduced in [Deardorff, 1970] and are based on averaging operators acting as low-pass filters. In the LES approach, vortex structures which are larger than the filter dimensions are resolved "exactly" (based on the solution of the Navier – Stokes equations). To resolve vortex structures of smaller sizes, additional (subgrid) relations are used. Therefore, the resources required to implement LES are much less than for DNS. Thus, to calculate turbulence away from solid walls, the number of grid cells required to perform LES increases with increasing Reynolds numbers and is proportional to $Re^{0.4}$ which is not so high compared to the DNS case [Гарбарук и др., 2012]. However, both LES and DNS have similar grid requirements near the walls. The number of cells required to simulate 3D isotropic flows is proportional to $Re^{1.8}$ [Гарбарук и др., 2012].

The computational grid employed in solving the Navier – Stokes equations typically comprises subdomains that exhibit varying values of the spatial step within the grid. In the references, the solution of the Navier – Stokes equations on grids with low spatial resolution (in its entirety or partially within the modeling domain) is called Implicit LES (ILES) modeling. The ILES technology is based on the fact that the inherent dissipation of the numerical method can be used instead of an explicit subgrid model [Ritos et al., 2018].

Numerical methods for applying ILES must provide high resolution and nonlinear stability while ensuring monotonicity or other physical/mathematical principles [Laney, 1998]. Without these conditions, which ensure (at least) second-order accuracy, the obtained results do not have the property of "high resolution" [Rider, Margolin, 2003].

Currently, ILES-modeling can be carried out using several approaches (see [Adams, Hickel, 2009]). The research [Kawamura, Kuwahara, 1984] represented one of the initial attempts to address the Navier – Stokes equations on a grid that did not have sufficient resolution; high resolution was only achieved in the boundary layer and the wake. Instead of referring to the method as ILES, another term was utilized in [Kawamura, Kuwahara, 1984]: the "direct integration" of the Navier – Stokes equations.

Although the ILES-approach is less computationally intensive than DNS, modeling flows at sufficiently high Reynolds numbers is technically challenging. Nevertheless, results on ILES- and DNS-modeling of internal and external flows at low Reynolds numbers are available in the literature. Direct numerical modeling is used to study turbulent flows because it eliminates the closure problem inherent in the RANS equations.

For low Reynolds numbers (about 10^3) a 3D cylindrical surface section is a canonical object for numerical simulation where the DNS- or LES-approaches can be used. The potential to reproduce various physical elements of the flow, such as the creation of wake vortices, the separation of the laminar boundary layer, and the development of shear layers (including the Karman vortex street), as it transitions into the turbulent flow zone, clarifies the interest in this task.

The results of the numerical simulation for Re = 3900 can be found, for example, in [Wissink, Rodi, 2008] (see a literature review on numerical simulations in [Molochnikov et al., 2019]). For the given value of the Reynolds number, some studies are also based on the Reynolds-averaged Navier – Stokes equations (see [Parnaudeau et al., 2008], for example).

Experimental data for the flow around the cylinder at Reynolds number Re = 3900 are presented in [Molochnikov et al., 2019; Parnaudeau et al., 2008]. Behind the grid of cylinders, it is possible to reproduce the flow conditions near isotropic turbulence [Stewart, Townsend, 1951]. A parallel

configuration of cylinders allows for the reproduction of flow conditions that exhibit 2D isotropic turbulence (in the direction of the lattice axis, the flow may be considered free of gradients).

In standard LES, physical theories of homogeneous isotropic turbulence are used to define subgrid models within the context of the theory proposed by A. N. Kolmogorov [Pope, 2000]. Although homogeneous isotropic turbulence conditions are only achieved in specific experimental studies, the spectral characteristics of flow around isolated bodies, particularly a cylindrical surface section, are traditionally compared in references to A. N. Kolmogorov's $-\frac{5}{3}$ law. Furthermore, the results derived from the modeling can be utilized to refine the LES model.

The spatio-temporal energy characteristics of the turbulent signal (velocity vector components) can be estimated using the Proper Orthogonal Decomposition (POD) of the velocity field components in a flow section [Holmes et al., 2012]. In references, the POD analysis is commonly known as modal analysis. A specific concept regarding the time-frequency characteristics of modal analysis is presented by Spectral Proper Orthogonal Decomposition (SPOD) [Sieber et al., 2016]. Geometric patterns illustrating the distribution of energy inhomogenity (relief) across a separated set of frequency characteristics (modes) offer a general insight into the properties of the averaged velocity field in the turbulent flow area.

Detailed information about the spectral characteristics of the flow is provided by spectral analysis based on the Fourier transform of the sampled signal. Kolmogorov's $-\frac{5}{3}$ law refers to the estimation of the Energy Spectral Density. Many studies also estimate the Power Spectral Density (PSD), which is determined by the ratio of the ESD in the temporal domain to the exposure time. Despite the differences in dimensions between the ESD and PSD characteristics, they exhibit identical distributions, differing only in the amplitude of the oscillations in the spectrum.

An examination of the dimensionality of the expression used to estimate the spatial energy spectral density (ESD) based on A.N. Kolmogorov's $-\frac{5}{3}$ law reveals that a similar dimensionality exhibits the spectral characteristic obtained through the spatial Fourier transform for instantaneous energy (instantaneous velocity squared). As highlighted above, when sampling a signal in the temporal domain, result of the Fourier transform (concerning the time coordinate) the instantaneous energy (which is determined by the second degree of fluctuations of the flow velocity vector components) is dimensionally consistent with the -2 law. This paper introduces an alternative spectral assessment of signal power, which is distinct from the Power Spectral Density (PSD) approach. This alternative method utilizes the Fourier transform applied to the third power of the signal, specifically focusing on the fluctuations of the velocity vector components. It is important to highlight that T. Karman suggested utilizing the third degree of the turbulent signal in addressing the issue of closing the Karman – Howarth equation [Karman, Howarth, 1938]. Drawing upon the theories proposed by A. N. Kolmogorov, this study demonstrates that the reference frequency spectrum of the third degree of the temporal sample of the signal (a component of the velocity vector) aligns with the distribution law of $-\frac{5}{2}$.

As an example, estimates of the energy spectrum for the transverse velocity vector component are provided for the incompressible flow around a 3D circular cylinder at the Reynolds number of 3900. The assessment of spectral characteristics is performed on data acquired through numerical modeling of the flow in the ANSYS Fluent program. The Navier – Stokes equations were resolved on a grid that delivered high resolution in the boundary layer area and the nearby region (on the order of the cylinder's diameter) of the wake behind the cylinder. In regions where the computational grid lacks sufficient resolution, larger cells serve the purpose of spatial averaging. Thus, instead of DNS, this research utilized the term ILES (or "direct integration" according to the terminology of [Kawamura, Kuwahara, 1984]). The spectral properties of the flow are assessed in the MATLAB code through the

discrete Fourier transform applied to the signal sampled in the time domain. In this paper, the POD method is used to estimate the spatio-temporal structure of flow based on the simulation results.

2. Spectrum of signal

2.1. Fourier transform of the first power of the signal

Spectral analysis for a time-limited signal $u(t)$ (fluctuations of velocity vector components) in the range $-\frac{T}{2} \leqslant t \leqslant \frac{T}{2}$ is carried out through the Fourier transform [Prandoni, Vetterli, 2008]:

$$\widetilde{u}(\omega) = \int_{-T/2}^{T/2} u(t) e^{-i\omega t}\, dt,$$

where $\omega = 2\pi f$, f is the frequency.

Using Parseval's theorem allows for the determination of the signal ESD [Lathi, Ding, 2010]:

$$E_D(\omega) = |\widetilde{u}(\omega)|^2. \tag{1}$$

In the references, the PSD estimation is also employed [Lathi, Ding, 2010]:

$$P_D(\omega) = \frac{E_D(\omega)}{T}. \tag{2}$$

Equations (1) and (2) suggest that the ESD and PSD distributions possess analogous spectral distributions, differing solely in terms of amplitude.

2.2. Fourier transform of the second power of the signal

For a continuous-time real signal $u(t)$, the energy is defined by the expression

$$E_\infty = \int_{-\infty}^{\infty} U(t)\, dt,$$

where $U(t) = u^2(t)$. In [Kusyumov et al., 2023] the Energy of Signal Spectrum (ESS) estimation was introduced to determine the energy properties of the signal:

$$E_S(\omega) = |\widetilde{U}(\omega)|, \tag{3}$$

where

$$\widetilde{U}(\omega) = \int_{-T/2}^{T/2} U(t) e^{-i\omega t}\, dt. \tag{4}$$

It is possible to establish the relationship between the energy of the signal $E_S(\omega)$ and the estimation of the E_∞. From the definition of the Fourier transform

$$\widetilde{U}(\omega) = \int_{-\infty}^{\infty} U(t) e^{-i\omega t}\, dt,$$

taking into account (3) and (4), it follows that

$$E_S(0) = |\widetilde{U}_\infty(0)| = |E_\infty|.$$

Consequently, the ESS may be regarded as the signal energy spectrum. The bandwidth of the signal $U(t)$ is two times that of the signal $u(t)$ [Lathi, Ding, 2010].

In addition, the Fourier transform can be introduced to evaluate the spatial distribution of the $u(x)$ spatial signal $\left(\text{in the range } -\frac{X}{2} \leqslant x \leqslant \frac{X}{2}\right)$:

$$E_S(k) = |\widetilde{U}(k)|,$$

where k is the wave number. The function $\widetilde{U}(k)$ is defined by the spatial Fourier transform:

$$\widetilde{U}(k) = \int\limits_{-X/2}^{X/2} U(x)e^{-2ixk}\,dx.$$

Here $U(x) = u^2(x)$.

From the analysis of expressions for ESD, PSD, and ESS, it can be concluded that these characteristics are derived from the Fourier transforms of the signal written in general form as

$$\mathrm{Sig}_m(t) = u^m(t). \tag{5}$$

In this context, it is defined that $m = 1$ for ESD, PSD, while $m = 2$ for ESS.

2.3. Fourier transform of the third power of the signal

Based on the statistical theory of isotropic turbulence, the connection between the second ($B_{LL}(r, t)$) and the third ($B_{LL,L}(r, t)$) correlation functions is defined by the Karman – Howard equation [Karman, Howarth, 1938; Monin, Yaglom, 1975]. Here r and t are the spatial and temporal coordinates, respectively. Since the Karman – Howarth equation is not closed, various authors have suggested hypotheses to establish the connection between the functions $B_{LL}(r, t)$ and $B_{LL,L}(r, t)$. In [Karman, Howarth, 1938], the simplest self-similarity hypothesis is proposed, suggesting that

$$B_{LL}(r, t) \sim v^2(t), \quad B_{LL,L}(r, t) \sim v^3(t). \tag{6}$$

The intensity of turbulence can be considered as the scaling function $v(t)$ [Monin, Yaglom, 1975]:

$$v(t) \sim \sqrt{B_{LL,L}(0, t)} = \sqrt{\overline{u}^2},$$

where $\overline{u}^2$ is defined as the probability-theoretic average over the corresponding statistical ensemble. From this expression it follows that the second correlation function at $r = 0$ determines the average energy of the signal. In [Kusyumov et al., 2020], a more general relationship between correlation functions was offered:

$$B_{LL,L}(r, t) \sim r^q B_{LL}^{3/2}(r, t), \tag{7}$$

where $q = \mathrm{const}$.

From expressions (6) and (7), it can be concluded that the third correlation function is characterized by the third degree of fluctuations of the components of the velocity vector. Therefore, in addition to the spectral characteristics of $\mathrm{Sig}_1(t)$ (ESD, PSD) and $\mathrm{Sig}_2(t)$ (ESS), one can consider the

spectrum of $\mathrm{Sig}_3(t)$. Assuming $m = 3$ in (5), we estimate the spectrum of the signal cubed [Kusyumov, Kusyumov, 2024]:

$$W(t) = u^3(t).$$

Using the Fourier transform, one can define the spectral function

$$P_S(\omega) = |\widetilde{W}(\omega)|,$$

where

$$\widetilde{W}(\omega) = \int_{-T/2}^{T/2} W(t) e^{-i\omega t}\, dt.$$

In [Kusyumov, Kusyumov, 2024] it was proposed to consider the function $\mathrm{Sig}_3(t) = W(t)$ as an alternative estimate of the instantaneous signal power. The rationale behind this interpretation lies in the observation that one of energy characteristics of the aircraft (power), is proportional to the cube of the speed. This refers to either the flight speed of an aircraft or the main rotor tip speed of a helicopter [Johnson, 2013]. In this context, the function $\widetilde{W}$ may be regarded as the Power Signal Spectrum (PSS).

3. Reference spectral estimations of signal energy and power

A specific application that employs the spectral features of the ESD and PSD signals, identified as $E_D(\omega)$ and $P_D(\omega)$, respectively, is aimed at analyzing the velocity pulsation spectrum for bluff bodies. Traditionally, the ESD and PSD characteristics derived from modeling are compared against the spectral distribution defined by the $-\frac{5}{3}$ law of A. N. Kolmogorov (K41 law, [Kolmogorov, 1991]). Recent research [Ma et al., 2025] explored K41 law scaling in bubble-induced turbulence.

The K41 law was formulated by A. N. Kolmogorov for the inertial subrange of the spectrum within the context of the statistical theory of turbulence. It is based on two hypotheses that determine the spectral characteristics of turbulent flow in the inertial subrange of the spectrum and is based on two hypotheses. In light of the comments made in [Monin, Yaglom, 1975], the similarity hypotheses of A. N. Kolmogorov can be stated in a simplified formulation.

The first similarity hypothesis. In the case of the high Reynolds number, the multidimensional probability distributions in the spatio-temporal area exhibiting locally isotropic turbulence are uniquely specified by the following parameters: the rate of dissipation of turbulence energy ϵ and the coefficient of kinematic viscosity ν.

Second similarity hypothesis. Within the energy regime of the corresponding turbulent flow, the key process is the transfer of energy to movements at smaller scales due to the influence of inertial forces, without any significant conversion of energy into heat. Consequently, the statistical patterns associated with this scale interval should, evidently, remain unaffected by the viscosity coefficient ν.

Based on these hypotheses and the statistical theory of turbulence, A. N. Kolmogorov derived the reference $-\frac{5}{3}$ law for the spatial energy spectrum:

$$E_{ij}(k) = \alpha_{ij} \epsilon^{2/3} k^{-5/3}.$$

For isotropic flows $\alpha_{ij} = \alpha_i \delta_{ij}$, where δ_{ij} is the Kronecker symbol; $\alpha_1 = \alpha_2 = \alpha_3 \sim 0.5$ (constant of A. N. Kilmogorov). Note that the dimension of the $E_{ij}(k)$ coincides with the dimension of the function $E_S(k)$. Therefore, the spatial spectrum $E_S(k)$, can be compared to the $-\frac{5}{3}$ law of A. N. Kolmogorov.

In [Tennekies, Lumley, 1972], the reference energy spectrum in the temporal domain was derived proceeding from the $-\frac{5}{3}$ law through the application of the statistical theory of turbulence:

$$\mathcal{E}_{ij}(\omega) = \beta_{ij}\epsilon\omega^{-2}, \tag{8}$$

where $\beta_{ij} = \beta = \alpha^{3/2}$. Note that in [Tennekies, Lumley, 1972] $\alpha = 1.5$ was accepted, hence $\beta \approx 0.84$ ($\alpha = 0.5$ for $\beta \approx 0.35$).

The similarity hypotheses of A. N. Kolmogorov and the dimension of the temporal spectrum derived from the Fourier transform of the velocity square can yield an expression that is similar to (8). From the $-\frac{5}{3}$ law, it follows that the reference spatial spectrum $E_{ij}(k)$ of the signal energy is determined by the energy dissipation rate ϵ and the wave number k. It can be assumed that in the temporal domain, the reference energy spectrum is determined by the energy dissipation rate ϵ and the frequency ω. Based on this assumption, the expression (8) was obtained in [Kusyumov et al., 2023] disregarding the constant β.

To obtain a reference spectrum estimate Π_{ij} of the turbulence power, an assumption is made: the similarity hypotheses of A. N. Kolmogorov are deemed suitable for estimating the signal power spectrum, i. e., Π_{ij} is a function of ϵ and ω composition. Then, through the dimensional analysis of the Fourier transform of $W_{ij}(t) = u_{ij}^3(t)$ (where $u_{ij}(t)$ represents the components of the velocity vector), it can be concluded that the reference power spectrum is defined by the expression

$$\Pi_{ij}(\omega) = \sigma_{ij}\epsilon^{3/2}\omega^{-5/2}, \tag{9}$$

where $\sigma_{ij} = \text{const}$.

Reference estimates $\mathcal{E}(\omega)$ and $\Pi(\omega)$ are employed below for comparison with the spectral distributions $E_S(\omega)$ and $P_S(\omega)$ obtained by modeling the flow around a section of a circular cylinder.

4. Numerical simulation

4.1. Computation mesh

For the simulation, a 3D circular cylinder section was examined. The flow conditions aligned with the Reynolds number $\text{Re} = \frac{V_\infty d}{\nu} = 3900$, where V_∞ is the free-stream velocity, d is the cylinder diameter, and ν is the kinematic viscosity coefficient. The simulation task was solved using the ANSYS Fluent code based on the direct integration (ILES approach) of the unsteady incompressible Navier–Stokes equations.

The computation domain (Fig. 1) was a rectangle with dimensions $20d \times 10d \times \pi d$. The coordinates in the longitudinal and normal directions are indicated as x, y, and z represents the transverse coordinate. In investigations with a related problem formulation (for Re = 3900), the dimensions of the computational domain along the x and y axes vary significantly: from $20d$ along the x axis and from $7d$ along the y axis (see, for example, the review in [Rajani et al., 2016]). In this research, the dimensions of the longitudinal and normal axes ($20d \times 10d$) are similar to [Snyder, Degrez, 2003]. The distance from the inlet face to the cylinder axis was $5d$. The transversal dimension $l_z = \pi d$ was adopted following the recommendations stated in [Kravchenko, Moin, 2000; Ma et al., 2000]. At the inlet boundary (as well as at the upper and lower boundaries), a uniform flow field was defined with the velocity vector $(u, v, w)^T = (1, 0, 0)^T V_\infty$. The outlet boundary utilized the "pressure outlet" condition, which is integrated into the ANSYS Fluent package.

Two kinds of boundary conditions are usually adopted at the lateral boundaries to approximate an infinite span length in numerical studies [Jiang et al., 2017], i. e., the "periodic" (for simulating

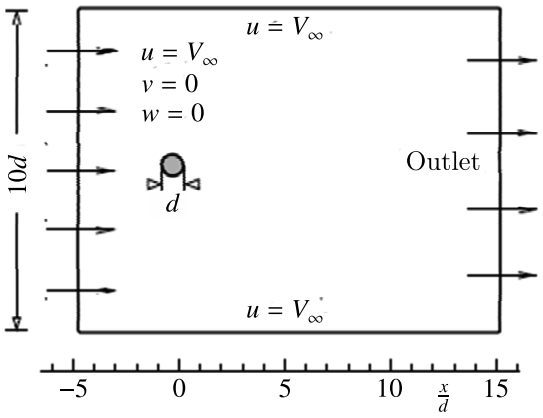

Figure 1. Scheme of the computational domain

the wake structures above the critical Re number) and the “symmetry”. The “symmetry” conditions were implemented in the present work on the side faces of the computational domain (orthogonal to z coordinate). The computational grid was created in the commercial ANSYS ICEM software and was refined in the direction normal to the cylinder surface.

In different studies applying the DNS technique, the computational grid consists of several million cells. In particular, in [Wissink, Rodi, 2008], modeling was carried out for several computational grids with cell numbers ranging from $10 \cdot 10^6$ (Case A) to $500 \cdot 10^6$ (Case E).

As mentioned in the introduction, the quantity of cells $N_{3/3}$ necessary for simulating 3D isotropic turbulent flow (in three directions) is directly proportional to $\mathrm{Re}^{9/4}$. For the considered task, the flow is gradient-free (in the integral sense) with respect to the z-axis. Therefore, the flow can only exhibit isotropy in two directions (in the directions of the x and y axes). The total number of cells in this situation can be regarded as proportional to the value $N_{2/3} \sim n_z \mathrm{Re}^{3/2}$, where n_z denotes the number of cells in the z direction. From the review of the literature, it can be concluded that the advised cell size in the z-axis direction is significantly larger than the wall cell size in the x and y axis directions. In this study, $n_z = 40$ has been selected, which specifically aligns with the recommendations outlined by [Kravchenko, Moin, 2000; Ma et al., 2000]. Hence, the required number of cells in the computational grid (at Re = 3900) can be estimated as $N_{2/3} \sim 40 \cdot 3900^{3/2} \approx 10^7$. This value approximately aligns with the Case A grid as referenced in [Wissink, Rodi, 2008]. The number of cells in the computational grid in this work also corresponds to the obtained estimate $N_{2/3}$.

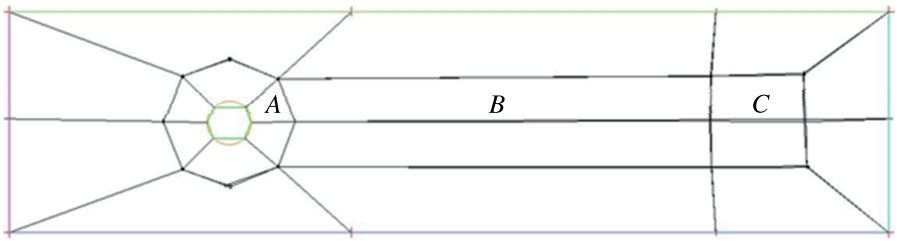

Figure 2. Blocking of the computational grids

Two computational hexa-grids consisting of $12 \cdot 10^6$ (Grid I) and $16 \cdot 10^6$ (Grid II) elements were created to study grid independence. The blocking of the computational grids is shown in Fig. 2. To resolve the boundary layer, the computational mesh was refined near the cylinder surface: the size of the first cell normal to the surface is about $10^{-3}d$.

Table 1 illustrates the parameters of the computational grids in regions neighboring the symmetry plane. The parameters provided are relevant to the top segment of the block structure (the parameters for the bottom segment are alike).

Table 1. Parameters of the computational grid in the direction of the coordinate axes of the polar (θ, r, z) and Cartesian (x, y, z) coordinate systems

Grid	$n_\theta \times n_r \times n_z/L_A$	$n_x \times n_y \times n_z/L_B$	$n_x \times n_y \times n_z/L_C$	l_z	Grid size
I	$60 \times 150 \times 40/d$	$500 \times 60 \times 40/10d$	$100 \times 60 \times 40/2d$	πd	$12 \cdot 10^6$
II	$60 \times 150 \times 40/d$	$900 \times 60 \times 40/10d$	$100 \times 60 \times 40/2d$	πd	$16 \cdot 10^6$

Zone A presents the calculation parameters in terms of azimuthal θ, radial r and transverse coordinates. In zones B and C, the number of nodes is represented along the x, y, and z coordinate axes. The parameters L_A, L_B, and L_C define the sizes of the zones.

Table 2 illustrates the distributions of cell sizes in zones A, B, and C for Grids I and II along x and y. A similar mesh size was applied in references [Mohammad et al., 2010; Beaudan, Moin, 1994; Jiang, Cheng, 2021]. In the vicinity of the near wall, the velocity gradients in the x and y directions are greater than the local gradients observed along the z-axis.

Table 2. Cell size distributions along x and y axes

Direction	Grid	Zone A	Zone B	Zone C
x-axis	I	$0.00125d \div 0.005d$	$0.005d \div 0.02d$	$0.02d \div 0.022d$
	II	$0.00125d \div 0.005d$	$0.005d \div 0.01d$	$0.01d \div 0.022d$
y-axis	I, II	$0.002d \div 0.015d$	$0.01d \div 0.03d$	$0.014d \div 0.035d$

The cell sizes of the computational grid can be assessed in relation to the Kolmogorov length scale [Monin, Yaglom, 1975]:

$$\frac{\eta}{L} = \mathrm{Re}^{-3/4}, \tag{10}$$

where L is the integral linear scale, commensurate with the size of the modeling domain.

Different techniques can be employed to estimate the value of L. In statistically inhomogeneous directions, physical parameters like channel width, boundary layer thickness, or mixing layer thickness dictate the largest scales [Moin, Mahesh, 1998]. In instances of flow through channels (or pipes), it is assumed that L equals half the characteristic size of the system: the half-width of the channel (or the radius of the pipe) [Coleman, Sandberg, 2010]. This approach, especially for channels, recognizes the existence of two regions that introduce disturbances into the flow, namely, the two opposing walls of the channel. In the flow around the cylinder, disturbances are introduced when the flow separates at the two opposite poles of the cylinder's surface (upper and lower). At the end of the recirculation zone, paired vortices emerge from the shear layers, which ultimately contributes to the development of the Karman vortex street. Assuming

$$L = \frac{d}{2}, \tag{11}$$

from (10) one can derive the relation for a prior estimate of the Kolmogorov length scale:

$$\eta \sim \frac{d}{2}\,\mathrm{Re}^{-3/4}. \tag{12}$$

The Kolmogorov length scale, represented by η, is generally estimated as the minimum scale that must be resolved. One should note that estimate (12) fails to account for the effect of body

shape on the disturbances introduced into the flow. In particular, for the Reynolds number Re = 3900, the expression (12) gives that the Kolmogorov length scale η is approximately $0.001d$. However, spectral DNS reveals a commendable consistency with experimental findings, even in the absence of Kolmogorov-scale resolution. Generally, the minimum length scale that needs to be resolved is greater than the Kolmogorov length scale [Moser, Moin, 1984; Kim et al., 1987]. For instance, [Moser, Moin, 1984] observed that most dissipation within a curved channel occurs at scales larger than 15η. Nevertheless, expression (12) can be used to provide an approximate assessment of the computational grid quality and, in particular, to evaluate the wall size of the cells. Considering this viewpoint, the wall cell sizes for all the discussed variants of the computational grid are comparable to the estimate (12).

Generally, the resolution (measured in Kolmogorov scale units) within the modeling domain for isotropic turbulence ought to be as estimated by [Parnaudeau et al., 2008]:

$$\Delta x = 4.5\eta, \quad \Delta y = 4.5\eta. \tag{13}$$

Furthermore, Table 2 indicates that the resolution of the computational grids in zone A along the longitudinal x-axis is consistent with the estimate (13). The resolution along the y-axis satisfies condition (13) in the neighborhood of the cylinder surface. Consequently, it may be concluded that in zone A and to some extent at the onset of zone B, the spatial resolution of the computational grids is approximately suitable for the implementation of DNS. For the rest of the computational domain, the modeling is conducted using the direct integration (ILES) approach.

The assessment of the step Δz of the computational grid can be inferred from the outcomes presented by [Roshko, 1993; Williamson, 1996], based on experimental results obtained by various authors. As stated by [Williamson, 1996], the wavelength of vortices within a shear layer is defined by two distinct scales:

a) $\frac{\lambda_{ZSL}}{d} \sim \frac{25}{\sqrt{\mathrm{Re}}}$ for vortices within a detached shear layer;

b) $\frac{\lambda_{ZK}}{d} \approx \frac{\lambda_K}{5d} \sim 1$ for vortices in the wake (where λ_K is the wavelength of the Karman vortices).

By setting $\lambda_z = 5\lambda_{ZSL}$, one can derive an estimate for the minimum length of the cylinder section within the range of $3900 \leqslant \mathrm{Re} < 100\,000$:

$$l_z = \frac{125d}{\sqrt{\mathrm{Re}}}.$$

For Re = 3900, it can be inferred from this ratio

$$l_z = 2d,$$

which matches the accepted transverse size of the modeling region $l_z = \pi d$ (see Table 1).

As stated by [Cao et al., 2020], the size of the cell along the z-axis in the shear layer is defined by the ratio $\Delta z \sim \frac{\lambda_{ZSL}}{6}$. From this it follows that the number of nodes in the computational grid is established by the ratio:

$$n_z \sim \frac{l_z}{\Delta z} = 30.$$

The obtained value is less than the number of the computational grids nodes $n_z = 40$, employed in this study.

4.2. Numerical simulation results

The Navier – Stokes equations were solved using ANSYS Fluent code, employing the SIMPLE algorithm with second-order spatial discretization and the first order-time discretization. The time step applied in the simulation is $\Delta t = \frac{0.0565d}{V_\infty}$. The time sample duration T must be adequate to guarantee a statistically stable condition. Typically, the value of T is established in proportion to the duration of the vortex formation cycle: $T = N_S T_K$, where T_K represents the period of the Karman street vortex shedding. The proportionality coefficient varies in references, for instance, from $N_S = 17$ [Jacob et al., 2018] to $N_S = 131$ [Ma et al., 2000]. In this research, $N_S = 100$ $\left(T \approx \frac{500d}{V_\infty}\right)$.

The sampling frequency corresponding to the time step is nearly 10^4. From the analysis of experimental and numerical modeling data presented in references for Re = 3900, it follows that the time step size is sufficient to reproduce the inertial subrange spectrum. Reducing the time step results in increased requirements for computational resources and does not yield a significant improvement in the accuracy of modeling within the inertial subrange. The same applies to the second-order temporal discretization. A numerical experiment employing temporal second-order discretization did not indicate any substantial alterations in the simulation outcomes. The error related to numerical integration in this case is proportional to $(\Delta t)^2$, and the upper frequency limit of the reproduced spectrum significantly exceeds the spectrum of the inertial range. The computation was executed on a 2x Intel Xeon Gold 6130 server, utilizing 28 cores and equipped with 64 GB of RAM. During each iteration time step, 20 sub-iterations were executed. The estimated duration for sample processing, roughly 10 000 steps, with the specified simulation parameters, was several weeks.

In order to assess the correctness of the wall step Δr along the normal to the surface, the maximum friction coefficient, $c_{f\max} = 0.092$, and the average friction coefficient, $c_{f\,\mathrm{av}} = 0.0256$, on the surface of the cylinder were determined. The value of c_f determines the parameter r^+ [Coleman, Sandberg, 2010]:

$$r^+ = \frac{u_\tau \Delta r}{\nu},$$

where

$$u_\tau = \left(\frac{\tau_w}{\rho}\right)^{1/2}, \quad \tau_w = c_f \frac{\rho V_\infty^2}{2}.$$

Expression for r^+ can be rewritten as

$$r^+ = \frac{\mathrm{Re}}{N}\sqrt{\frac{c_f}{2}}, \tag{14}$$

where $N = \frac{d}{\Delta r}$. Substituting $c_{f\max} = 0.092$ into (14) under the simulation conditions yields $r^+_{\max} = 1.04$, which ensures $r^+ \leqslant 1$ at the most part of the cylinder surface. For the average friction coefficient $c_{f\,\mathrm{av}} = 0.0256$ substituting into (14) gives $r^+_{\mathrm{av}} = 0.55$. Using relation (12), one can approximately estimate the value of the Kolmogorov length scale η derived from the results of numerical simulation. According to [Pope, 2000], the value η is defined by the expression

$$\eta = \left(\frac{\nu^3}{\epsilon}\right)^{1/4},$$

where ϵ denotes the rate of turbulent energy dissipation. One can express ϵ in terms of the integral scale [Monin, Yaglom, 1975]: $\epsilon \sim \frac{u_\tau^3}{\kappa L}$. From this, taking into account the expression for u_τ, it follows that

$$\eta \sim L\frac{\left(2^3\kappa^2\right)^{1/8}}{c_f^{3/8}\,\mathrm{Re}^{3/4}}. \tag{15}$$

Expression (15) includes the Karman constant $\kappa = 0.41$. Taking into account, as mentioned earlier, that the integral scale is determined by (11), from (15) one can derive

$$\eta \sim d\frac{\left(2^3\kappa^2\right)^{1/8}}{2c_f^{3/8}\,\mathrm{Re}^{3/4}}.$$

Substituting $c_{f\,\mathrm{av}}$ into this expression results in the Kolmogorov length scale $\eta \approx 0.004d$. Comparing the obtained value with the cell sizes in zones A, B, and C, one can assume that Grid II permits the reproduction of the spectrum of the inertial subrange in zone A and a significant part of zone B. For Grid I, the inertial range of the spectrum can be reproduced in zone A.

Figure 3 shows the distribution of the velocity vector magnitude in the plane of symmetry for Grids I and II.

For both cases in Fig. 3, one can distinguish shear layers that are shed alternately from the upper and lower cylinder surface. At the termination of the recirculation zone, the shear layers become unstable and initiate the formation of incipient vortices. In the considered section, shear layers create almost straight lines up to a distance $L_s = 2d$, similar to the flow visualization shown in [Parnaudeau et al., 2008]. At the distance $x = L_s$ downstream, one can observe the folding of shear layers. Ultimately, both shear layers generate a Karman vortex street, which manifests downstream as two cyclic vortex formations.

Figure 3 shows that in the vicinity of the cylinder surface (zone A and a part of zone B), the velocity distribution in the wake trailing the cylinder exhibits a nearly identical vortex flow structure due to the proximity of the parameters of the computational grids. Large vortex structures correspond to the Karman vortex street. In the distant regions of zones B and C, Grid II provides a more detailed structure of the velocity field.

Figure 4 presents the distribution of the longitudinal $u - V_\infty$ and transverse v, w components of the velocity vector in the symmetry plane for Grid I.

From Fig. 4, it follows that there are inhomogeneities both within and beyond the recirculation zone (approximately corresponding to the $L_s \times d \times l_z$) for all components of the velocity vector.

The integral characteristics obtained for Grids I and II were considered earlier in [Kusyumov et al., 2023] compared to experimental data from [Ong, Wallace, 1996; Kravchenko, Moin, 2000]. Some results of modeling the flow around an isolated cylinder for Grids I and II are presented in Table 3.

Table 3. Simulation results compared with experimental data

Grid	$\overline{c}_{xa}$	$-c_{pb}$	St	θ_{sep}
I	0.95 ± 0.03	0.92	0.226	84.3°
II	0.96 ± 0.03	0.88	0.224	84.8°
Experiment	0.99 ± 0.05	0.88 ± 0.05	0.215 ± 0.05	86 ± 2°

The average drag coefficient $\overline{c}_{xa}$ for an isolated cylinder, the minimum value of the pressure coefficient $-c_{pb}$, the separation angle θ_{sep}, and the Strouhal number St (based on the Karman vortex street frequency) for the transverse component v are in satisfactory agreement with experimental data [Kravchenko, Moin, 2000; Ong, Wallace, 1996]. The instantaneous values of $-c_{pb}$ and θ_{sep} are presented here without averaging. The Strouhal number in Table 3 was assessed at the point $\left(3d,\ 0,\ \frac{\pi d}{2}\right)$ for the transverse v component. According to experimental data [Kravchenko, Moin, 2000], the amplitude of the oscillations of the transverse component v exceeds that of the longitudinal component u at a similar point. Therefore, further spectral analysis of the time signal at a fixed point was performed

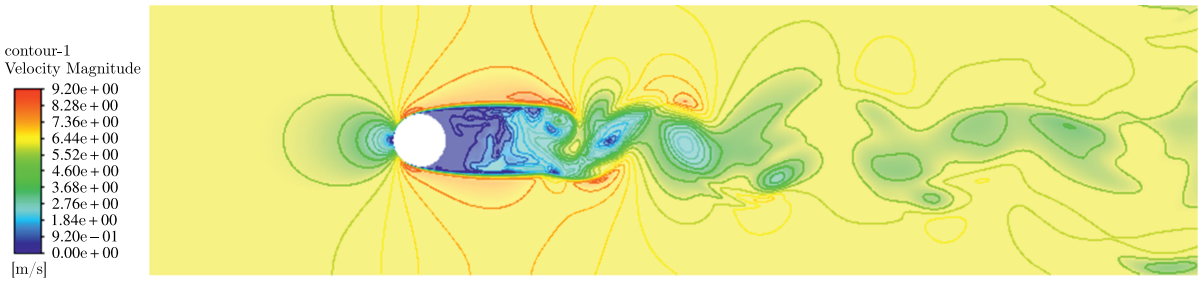

(a) I

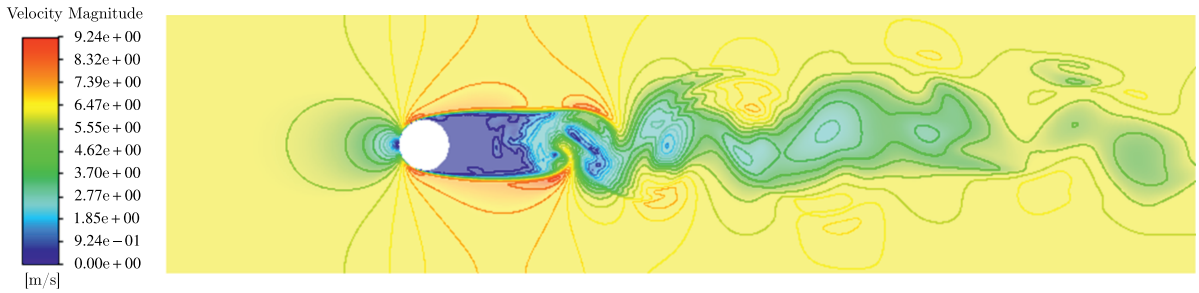

(b) II

Figure 3. Instantaneous velocity magnitude field in the symmetry plane for Grids I and II

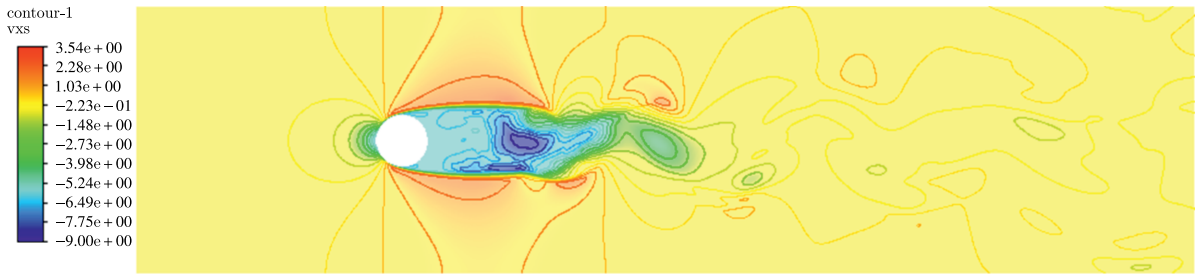

(a)

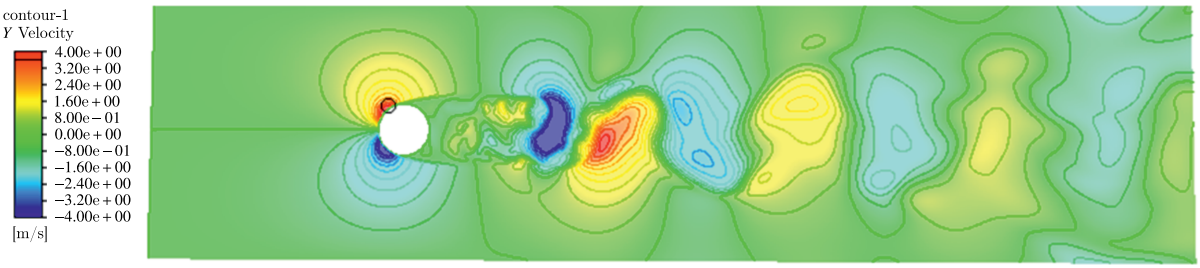

(b)

(c)

Figure 4. Distribution of current velocity vector components in the symmetry plane: a) $u - V_\infty$; b) v; c) w

for the v component. However, the time spectral characteristics of the u component were also examined using the POD analysis.

5. POD analysis of the velocity field

Dynamic structures in turbulent flows can interact and eventually vanish. Modal decompositions can be employed to extract these structures. The Proper Orthogonal Decomposition (POD) algorithm [Holmes et al., 2012] delivers a basis of modes that is optimal for analyzing the energy characteristics of the flow. The POD method is focused on maximizing the energy represented by a spatial mode distribution. For each mode, the spectral characteristics of the unsteady mode coefficients are also estimated. In this paper, POD is applied to analyze the longitudinal (u) and transverse (w) components of the velocity vector (u, v, w) obtained in the $y = 0$ plane of the cylinder wake. The choice of (u, w) vector for the POD analysis is determined by the features of the spectral characteristics. The direction of the w component aligns with the cylinder z-axis, along which the flow is gradientless. The total number of cells in the z-axis direction was ascertained (see Section 3) according to the experimental data outlined in [Williamson, 1996]. The number of cells along the cylinder z-axis that influence the spectral characteristics of the energy of the vector modes (u, w) is evaluated. The MATLAB program was developed to conduct the POD analysis utilizing the algorithm outlined in [Sieber et al., 2016].

The inner product for two arbitrary square integrable functions $u(\boldsymbol{x})$ and $v(\boldsymbol{x})$ is defined by the integral

$$\langle u(\boldsymbol{x}),\, v(\boldsymbol{x})\rangle = \int\limits_V u(\boldsymbol{x})v(\boldsymbol{x})\, dV,$$

where V defines the spatial region. Unsteady POD analysis is performed for N spatial fields (snapshots) of velocity vector components derived from either experiment (PIV data) or numerical (CFD) simulations. The decomposition of the velocity vector $\boldsymbol{u}$ for POD analysis is determined by the expansion into the average ($\overline{\boldsymbol{u}}$) and fluctuating ($\boldsymbol{u}'$) components:

$$\boldsymbol{u}(\boldsymbol{x},\, t) = \overline{\boldsymbol{u}}(\boldsymbol{x}) + \boldsymbol{u}'(\boldsymbol{x},\, t) = \overline{\boldsymbol{u}}(\boldsymbol{x}) + \sum_{i=1}^{N} a_i \Phi_i(\boldsymbol{x}),$$

where $\boldsymbol{x}$ is the coordinate vector and t is the time variable. Here $\Phi_i(\boldsymbol{x})$ are a dimensionless normalized basis of functions (modes), and the unsteady coefficients $a_i(t)$ (random functions) determine the energy properties of the modes. For N spatial images it is possible to determine the correlation matrix $\boldsymbol{R}$:

$$\boldsymbol{R}_{ij} = \frac{1}{N}\langle \boldsymbol{u}'(\boldsymbol{x},\, t_i),\, \boldsymbol{u}'(\boldsymbol{x},\, t_j)\rangle.$$

The unsteady coefficients $\boldsymbol{a}_i = [a_i(t_1), \ldots, a_i(t_N)]^T$ and mode energies λ_i are defined as eigenvectors and eigenvalues of the correlation matrix:

$$\boldsymbol{R}\boldsymbol{a}_i = \lambda_i \boldsymbol{a}_i.$$

The relative energy contribution of modes is determined by the dimensionless coefficients

$$\widetilde{\lambda}_i = \frac{\lambda_i}{\sum\limits_{i=1}^{N} \lambda_i}.$$

The projection of the snapshots onto the temporal coefficients yields the spatial modes:

$$\Phi_i(\boldsymbol{x}) = \frac{1}{N\lambda_i} \sum_{i=1}^{N} a_i(t_j)\boldsymbol{u}'(\boldsymbol{x}, t_j).$$

The Fourier Transform allows conversion of the time domain signal $\boldsymbol{u}'(\boldsymbol{x}, t)$ into the frequency domain

$$\boldsymbol{u}'(\boldsymbol{x}, f) = \sum_{i=1}^{N} A_i(f)\Phi_i(\boldsymbol{x}),$$

where

$$A_i(f) = \int_{-T/2}^{T/2} a_i(t)e^{-i\omega t}\, dt.$$

In this paper, the POD is applied to simulation data obtained in the wake of a cylinder: $N = 101$ snapshots of the longitudinal u and transversal w velocity vector components are collected. Figure 5 shows the instantaneous distributions of the u and w components in the $y = 0$ plane. The scanning region for SPOD analysis is indicated by a black frame downstream from the cylinder.

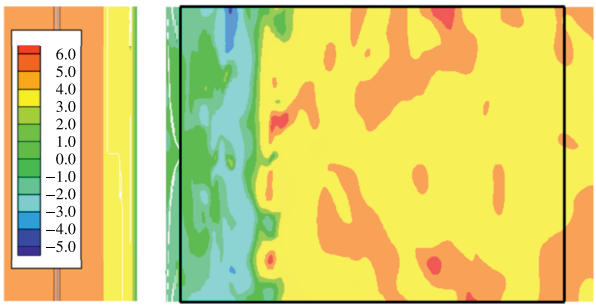

(a)

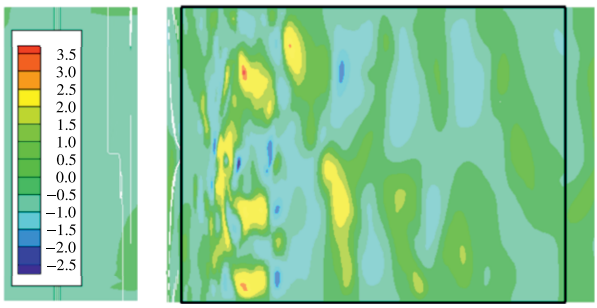

(b)

Figure 5. Instantaneous distribution of the u (a) and w (b) components of the flow velocity vector in the plane $y = 0$ (Grid II)

A data array of 300×100 elements of the u and w components was formed using interpolation in the Tecplot package for each time step. Since the number of points along the z-axis is restricted to 40 (interpolation is used to produce intermediate points), increasing the number of interpolation points along the z-axis will not increase the resolution of the spatial structure of the mode. Therefore, the size of the entire data array for the spatio-temporal analysis is $300 \times 100 \times 101$. In contrast to the pictures in Figs. 3 and 4, Fig. 5 does not display the regular structures that define the Karman vortex street. One

of the tasks of POD analysis in this work is the analysis of frequency characteristics of the modes $A_i(f)$ of the (u, w) vector to identify spectral regions corresponding to the Karman vortex street frequency.

According to [Sieber et al., 2016], the spatio-temporal (spatio-frequency) characteristics of the modes are determined by the filtering parameter N_f of the SPOD analysis. In this paper, the characteristics of the modes are presented by $N_f = 0$, which corresponds to the POD analysis.

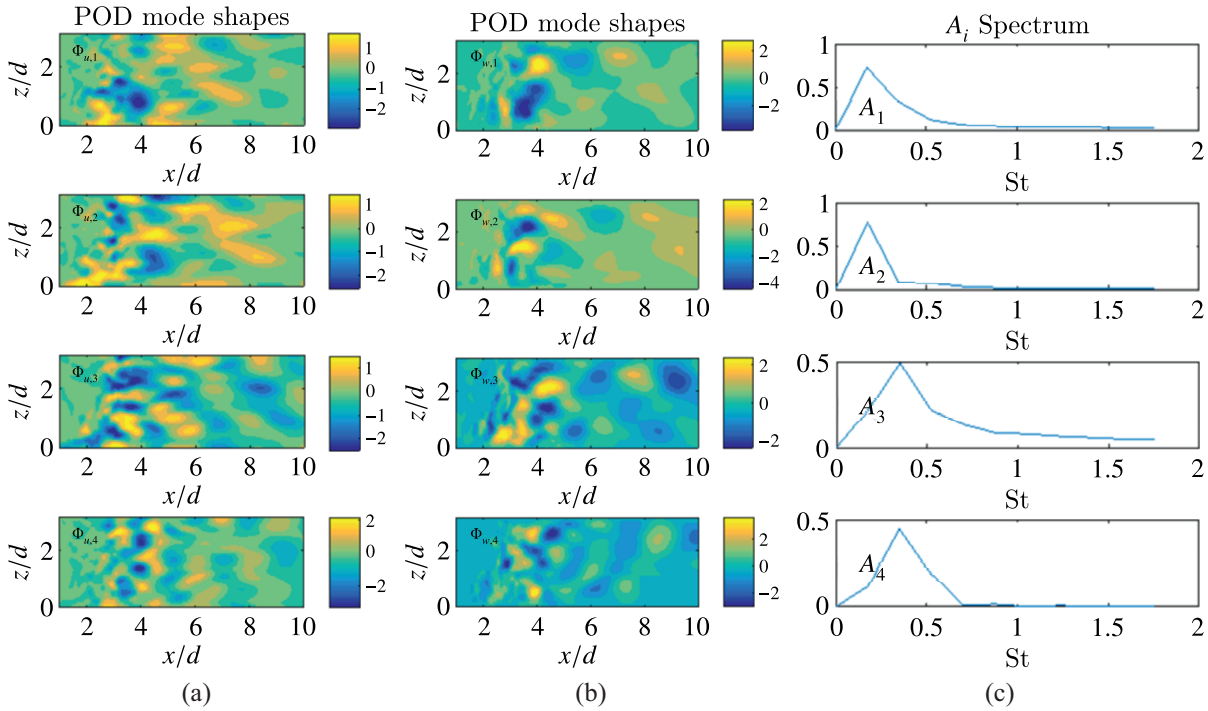

Figure 6. Spatial relief of the components u (a), w (b) of the velocity vector (u, w) and spectra (c) of the temporal coefficients of the first four modes for the Grid II

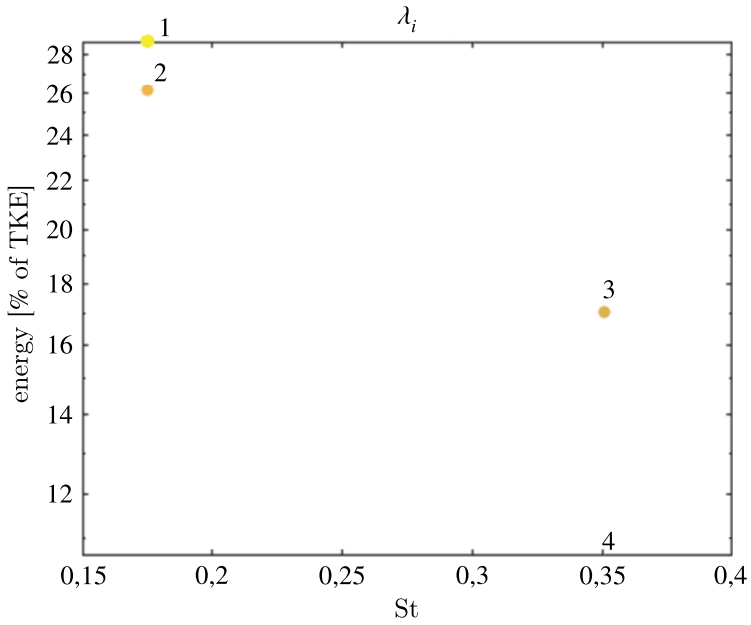

Figure 7. Discrete frequency-energy characteristics of the four most energetic modes of POD analysis for the Grid II

POD analysis was done for both the entire vector (u, w) and each component u and w individually. In the first case, the spatial mode vector $\Phi_i = (\Phi_{ui}, \Phi_{wi})$ is estimated and the unsteady coefficients $a_i(t)$ determine the mode energies λ_i for the velocity vector (u, w). In the second case, Φ_{ui}, λ_{ui} and Φ_{wi}, λ_{wi} are estimated for the "separated" vectors (u, 0) and (0, w), respectively.

Figure 6 shows the "spatial reliefs" of the first four most energy-intensive modes for the components (u, w) and the frequency characteristics of the coefficients A_i (depending on the Strouhal number St). For each of the presented modes, a discrete set of Strouhal numbers St_i can be determined from the condition $A_i(\mathrm{St}_i) = \max(A_i)$.

Analysis of the spatial relief of modes allows identifying regions of inhomogenities: "energy peaks" (yellow spots) and "energy dips" (dark blue spots). The highest concentration of relief inhomogenities for all modes is observed at $\frac{x}{d} > 2$ (in the distance, more than $3d$ from the cylinder center). The "smoothing of the relief" that is observed at distances larger than $6d$ is linked to the dissipation of turbulent energy. The smallest (about $0.1d$ in size) relief inhomogenities are noted for the third and fourth modes. Thus, there are no regular structures in the mode relief images, as well as in the images of instantaneous velocity fields in Figure 5. Figure 7 shows the discrete frequency-energy characteristics of the modes $\widetilde{\lambda}_i(\mathrm{St}_i)$.

From Fig. 7, it follows that the first mode is the most energy-intensive, despite the higher amplitude of the second mode $A_2(\mathrm{St}_2) > A_1(\mathrm{St}_1)$. In this case, the spectral range of the first mode significantly exceeds the spectral range of the second mode, which ultimately ensures a more significant energy contribution of the first mode.

Analysis of the spectrum of mode coefficients in Fig. 6, *c* reveals that the first and second modes have the greatest amplitudes and an approximately similar frequency range. The frequencies of these modes (the Strouhal numbers) are comparable to the frequency of the Karman vortex street. Thus, despite the lack of regular structures in the mode images, the spectral range corresponding to the Karman vortex street frequency is "inherited" by the modes frequency characteristics.

6. Spectral characteristics of the flow

Figures 8–10 illustrate the spectral properties of the transverse velocity v along the axial line at the coordinate $\left(3d, 0, \frac{\pi d}{2}\right)$, derived for a $16 \cdot 10^6$ grid through the Fourier transform of the temporal sample of the signal. Figure 8 represents the traditional (generally accepted) normalized evaluation of the distribution of the power spectral density $P_D(f)$ displayed on a logarithmic scale.

The normalized PSD function is given by

$$\overline{P}_D(\overline{f}) = \frac{P_D(\overline{f})}{V_\infty^2 T}.$$

Here $\overline{f} = \frac{f}{f_K}$ is the oscillation frequency normalized to the frequency f_K of the Karman vortex street.

The results of numerical simulation for Grid II are compared with references [D'Alessandro et al., 2016; Jiang, Cheng, 2021] and Kolmogorov's law $-\frac{5}{3}$. One should note that Fig. 8 presents the distributions that characterize the approximate range of variation of the $\overline{P}_D(\overline{f})$ spectrum, according to the data provided by [D'Alessandro et al., 2016; Jiang, Cheng, 2021], which utilized the LES and DES eddy-resolving models, respectively. In both cases, the computational meshes consisted of approximately $5 \cdot 10^6$ elements. The presented results were acquired at a similar location behind the surface of the cylinder.

The spectral distribution depicted in Figs. 8–10 contains regions representing the energy and inertial subranges. The solid oscillating line (gray) illustrates the full spectrum derived from the Fourier

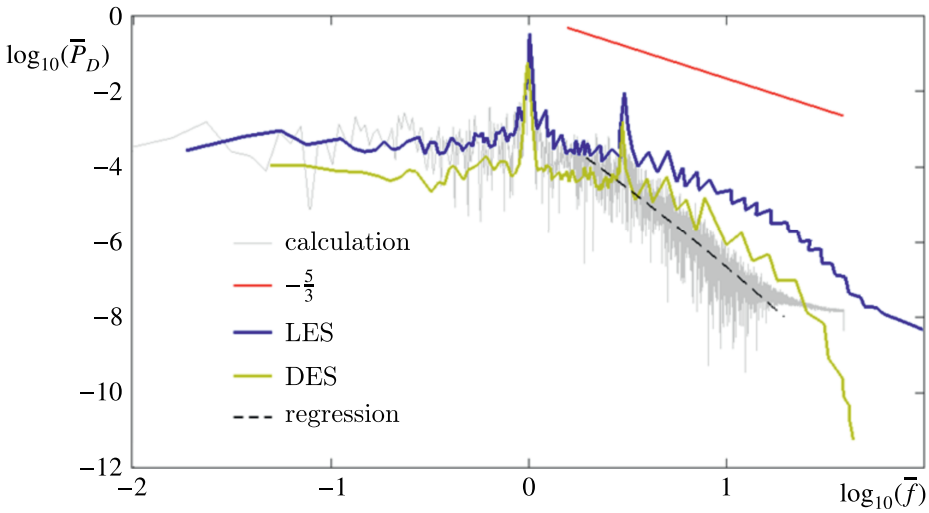

Figure 8. Distribution of $\overline{P}_D(\overline{f})$ for the transverse velocity v at the point $\left(3d,\ 0,\ \frac{\pi d}{2}\right)$

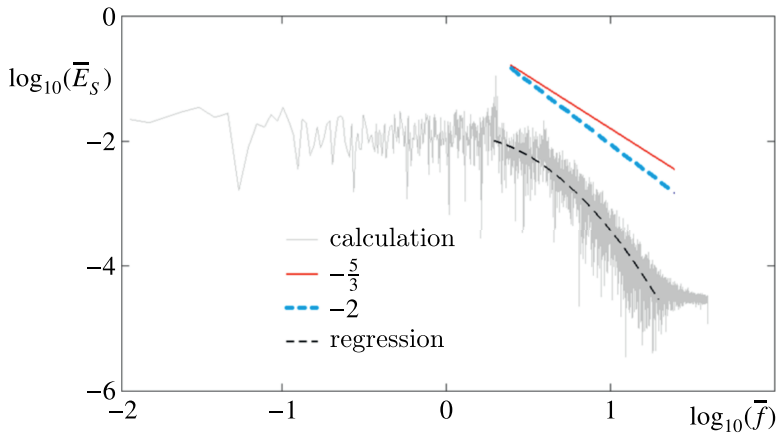

Figure 9. Distribution of $\overline{E}_S(\overline{f})$ for the transverse velocity v at the point $\left(3d,\ 0,\ \frac{\pi d}{2}\right)$

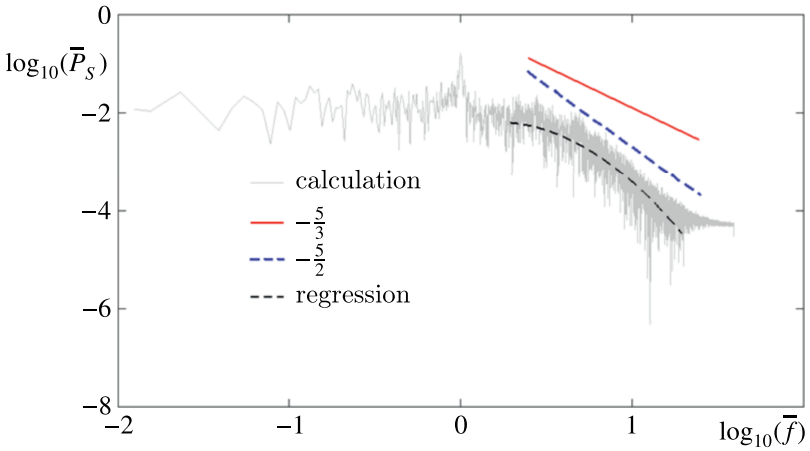

Figure 10. Distribution of $\overline{P}_S(\overline{f})$ for the transverse velocity v at the point $\left(3d,\ 0,\ \frac{\pi d}{2}\right)$

transform of the time-sampled signal. The second-degree polynomial, illustrated by the dashed line, was generated via regression analysis performed in Microsoft Excel, targeting the region that includes segments of the energy (low frequencies/large vortex structures) and inertial subranges.

The results obtained from the simulation in the energy subrange (low-frequency region) are consistent with the data provided in [Jiang, Cheng, 2021], which are based on the implementation of the LES model. In the energy subrange, notable peak values of the signal amplitude are identified at the frequency of the Karman track ($\overline{f} = 1$) and for the second harmonic ($\overline{f} = 3$), as conventionally documented in the literature. In the inertial subrange, the distribution $\overline{P}_D(\overline{f})$ agrees with the results of [D'Alessandro et al., 2016] obtained using the DES model.

Figures 9 and 10 provide alternative estimates for the energy spectral distribution (ESS) and the power spectral distribution (PSS) introduced in this study. The normalized $\overline{E}_S(\overline{f})$ function, employed for evaluating the energy spectrum (Fig. 9) is characterized by the expression below:

$$\overline{E}_S(\overline{f}) = \frac{E_S(\overline{f})}{V_\infty^2 T}.$$

The results of the numerical simulation of the energy spectrum for the transverse velocity ($i = j = 2$) are compared in Fig. 9 with Kolmogorov's law $-\frac{5}{3}$ and with the $\mathcal{E}_{22}(\omega)$ distribution.

From the presented CFD simulation data, it can be seen that in the elevated frequency range $\overline{E}_S(\overline{f})$ is in better agreement with the distribution $\mathcal{E}_{22}(\omega)$ compared to the $-\frac{5}{3}$ law.

Figure 10 shows the distribution of the normalized function $\overline{P}_S(\overline{f})$ in comparison with the law $-\frac{5}{3}$ by A. N. Kolmogorov and the dependence defined by expression (9). The normalized function $\overline{P}_S(\overline{f})$ is defined as

$$\overline{P}_S(\overline{f}) = \frac{P_S(\overline{f})}{V_\infty^3 T}.$$

From Fig. 10, it follows that the curve $\overline{P}_S(\overline{f})$ has a peak value corresponding to the frequency of the Karman vortex street.

In the inertial subrange, there are regions where the slope of the $\overline{P}_S(\overline{f})$ curve corresponds to both the $-\frac{5}{3}$ and $-\frac{5}{2}$ laws. In general, the gradient of the $\overline{P}_S(\overline{f})$ regression in the inertial subrange better agrees with the $-\frac{5}{2}$ law than with the $-\frac{5}{3}$ law.

7. Conclusion

The power and energy spectra are evaluated for a signal represented by the longitudinal or transverse components of the turbulent flow velocity vector. In addition to the power spectral density (as commonly defined), the instant energy spectrum, which is calculated by squaring the temporal sample of the signal, and the power spectrum, which is derived from a cubic relationship (alternative formulation), are estimated. Using Fourier transforms and taking into account Kolmogorov's hypothesis for homogeneous isotropic turbulence, it is shown that the reference spectral estimates of the instant energy and power of signal (in alternative formulation) are determined by the laws of -2 and $-\frac{5}{2}$, respectively.

As an application, ILES modeling of three-dimensional flow around a section of circular cylinder at Re = 3900 is studied numerically based on the unsteady incompressible Navier – Stokes equations. The simulation area in the x and y directions consists of several subareas that have differing cell sizes. Along the z-axis of the cylinder, the size of the cells remains constant. Estimates regarding the resolution of the computational grid along the x, y, and z axes are provided in comparison to reference data. It is shown that in the immediate vicinity downstream the cylinder surface, the size of the

computational grid cells corresponds to the requirements for performing Direct Numerical Simulation (DNS). In order to assess the spatio-temporal spectral properties of the flow, an analysis of the velocity fields is performed utilizing proper orthogonal decomposition (POD). It has been demonstrated that, even in the absence of consistent structures within the instantaneous representation of vector fields in the (x, z) plane and the mode images, the frequency characteristics of the modes exhibit spectral ranges that align with the Karman street frequency.

The analysis of the simulation results focuses primarily on the spectrum of transverse flow velocity in the vicinity of the wake behind the cylinder. It has been shown that the numerical results obtained from the traditional formulation of the power spectral density are largely consistent with the modeling data available in the literature, which relies on the use of eddy-resolving DES and LES models. The instantaneous energy spectrum of the signal obtained by simulation was compared with the $-\frac{5}{3}$ law of A. N. Kolmogorov and the -2 law. The distribution of the power spectrum (in an alternative formulation) was also compared with the $-\frac{5}{2}$ law.

References

Гарбарук А. В., Стрелец М. Х., Шур М. Л. Моделирование турбулентности в расчетах сложных течений: учебное пособие. — СПб.: Изд-во Политехн. ун-та, 2012. — 88 с.
Garbaruk A. V., Strelets M. Kh., Shur M. L. Modelirovanie turbulentnosti v raschetah sloznih techenii: uchebnoe posobie [Turbulence modeling in complex flow calculations: a teaching guide]. — Saint Petersburg: Politechn. un-t, 2012. — 88 p.

Adams N. A., Hickel S. Implicit large-eddy simulation: theory and application // Advances in turbulence XII / B. Eckhardt (eds.). — Springer Proceedings in Physics. — Vol. 132. — Berlin, Heidelberg: Springer, 2009. — P. 743–750.

Beaudan P., Moin P. Numerical experiments on the flow past a circular cylinder at a subcritical Reynolds number. — Technical report TF-62. — Thermosciences Division, Department of Mechanical Engineering, Stanford University, 1994.

Boris J., Grinstein F. F., Oran E., Kolbe R. New insights into large eddy simulation // Fluid Dyn. — 1992. — Vol. 10, No. 4–6. — P. 199–228.

Cao J., Tamura T., Kawai H. Spanwise resolution requirements for the simulation of high-Reynolds-number flows past a square cylinder // Computers & Fluids. — 2020. — Vol. 196. — 104320.

Cheng Z.-P., Qiu S.-Y., Xiang Y., Liu H. Quantitative features of wingtip vortex wandering based on the linear stability analysis // AIAA Journal. — 2019. — Vol. 57, No. 7. — P. 2694–2708.

Coleman G. N., Sandberg R. D. A primer on direct numerical simulation of turbulence — methods, procedures and guidelines. — Technical Report AFM-09/01a. — School of Engineering Sciences, University of Southampton, 2010.

D'Alessandro V., Montelpare S., Ricci R. Detached-eddy simulations of the flow over a cylinder at Re = 3900 using OpenFOAM // Computers & Fluids. — 2016. — Vol. 136. — P. 152–169.

Deardorff J. W. A numerical study of three-dimensional turbulent channel flow at large Reynolds numbers // J. Fluid Mech. — 1970. — Vol. 41, No. 2. — P. 453–480.

Dou H.-S. Origin of turbulence. Energy gradient theory. — Springer Nature Singapore Private Ltd, 2022. — 489 p.

Holmes H., Lumley J. L., Berkooz G., Rowley C. W. Turbulence, coherent structures, dynamical systems and symmetry. — 2nd ed. — Cambridge, England, U.K.: Cambridge University Press, 2012. — 386 p.

Jacob J., Malaspinas M., Sagaut P. A new hybrid recursive regularised Bhatnagar – Gross – Krook collision model for Lattice Boltzmann method-based large eddy simulation // Journal of Turbulence. — 2018. — Vol. 19, No. 11–12. — P. 1051–1076.

Jiang H., Cheng L. Large-eddy simulation of flow past a circular cylinder for Reynolds numbers 400 to 3900 // Physics of Fluids. — 2021. — Vol. 33. — P. 034119.

Jiang H., Cheng L., An H. On numerical aspects of simulating flow past a circular cylinder // International Journal for Numerical Methods in Fluids. — 2017. — Vol. 85. — P. 113–132.

Johnson W. Rotorcraft aeromechanics. — Cambridge University Press, 2013. — 927 p.

Karman Th., Howarth L. On the statistical theory of isotropic turbulence // Proceedings of the Royal Society London, Series A. — 1938. — Vol. 164, No. 917. — P. 192–215.

Kawamura T., Kuwahara K. Computation of high Reynolds number flow around a circular cylinder with surface roughness // AIAA pap. 84-0340. — 1984.

Kim J., Moin P., Moser R. Turbulence statistics in fully developed channel flow at low Reynolds number // Journal of Fluid Mechanics. — 1987. — Vol. 177. — P. 133–166.

Kolmogorov A. N. A refinement of previous hypotheses concerning the local structure of turbulence in a viscous incompressible fluid at high Reynolds number // J. Fluid. Mech. — 1962. — Vol. 13. — P. 82–85.

Kolmogorov A. N. The local structure of turbulence in incompressible viscous fluid for very large Reynolds numbers // Proceedings: Mathematical and Physical Sciences. — 1991. — Vol. 434 (1890). — P. 9–13.

Kraichnan R. H. On Kolmogorov's inertial-range theories // Journal of Fluid Mechanics. — 1974. — Vol. 62, No. 2. — P. 305–330.

Kravchenko A. G., Moin P. Numerical studies of flow over a circular cylinder at $\mathrm{Re}_D = 3900$ // Physics of Fluids. — 2000. — Vol. 12, No. 2. — P. 403–417.

Kusyumov A. N., Kusyumov S. A. About the analysis of turbulent signal pulsations // LXXVII Herzen readings. International Conference Proceedings. RGPU n.a. A. I. Herzen, Saint Petersburg. — 2024. — P. 310–314.

Kusyumov S. A., Kusyumov A. N., Romanova E. V. Spectral characteristics of three-dimensional flow around a circular cylinder // Russian Aeronautics. — 2023. — Vol. 66, No. 2. — P. 276–282.

Kusyumov A. N., Mikhailov S. A., Kusyumov S. A., Romanova E. V. Isotropic turbulence correlation functions modelling on the basis of Karman – Howarth equation // Journal of Physics: Conference Series. — 2020. — Vol. 1675. — 012010.

Laney C. B. Computational gasdynamics. — Cambridge University Press, 1998. — 632 p.

Lathi B. P., Ding Z. Modern digital and analog communication systems. — 4th edn. — New York: Oxford university press, 2010. — 912 p.

Lesieur M. P., Metais O. New trends in large-eddy simulations of turbulence // Annual Review of Fluid Mechanics. — 1996. — Vol. 28. — P. 45–82.

Long R. R. Do tidal-channel turbulence measurements support $k^{(-5/3)}$? // Environmental Fluid Mechanics. — 2003. — Vol. 3, No. 2. — P. 109–127.

Ma T., Tan S., Ni R., Hessenkemper H., Bragg A. D. Kolmogorov scaling in bubble-induced turbulence // Physical Review Letters. — 2025. — Vol. 134. — 244001. — P. 1–6.

Ma X., Karamonos G. S., Karniadakis G. E. Dynamics and low-dimensionality of a turbulent near wake // Journal of Fluid Mechanics. — 2000. — Vol. 410. — P. 29–65.

Margolin L., Rider J., Grinstein F. F. Modeling turbulent flow with implicit LES // J. Turbul. — 2006. — Vol. 7 (15). — P. 1–27.

Mohammad A. H., Wang Z. J., Liang Ch. Large eddy simulation of flow over a cylinder using high-order spectral difference method // Advances in Applied Mathematics and Mechanics. — 2010. — Vol. 2, No. 4. — P. 451–466.

Moin P. Progress in large eddy simulation of turbulent flows // AIAA pap. 97-0749. — 1997.

Moin P., Mahesh K. Direct numerical simulation: a tool for turbulence research // Annual Review of Fluid Mechanics. — 1998. — Vol. 30. — P. 539–578.

Molochnikov V. M., Mikheev N. I., Mikheev A. N., Paereli A. A., Dushin N. S., Dushina O. A. SIV measurements of flow structure in the near wake of a circular cylinder at Re = 3900 // Fluid Dynamics Research. — 2019. — Vol. 51, No. 5. — 055505.

Monin A. S., Yaglom A. M. Statistical fluid mechanics. Vol. II: Mechanics of Turbulence. — Cambridge, Massachusetts: MIT Press, 1975. — 896 p.

Moser R. D., Moin P. Direct numerical simulation of curved turbulent channel flow. — NASA TM 85974. Also, Rep. TF-20. — Stanford, California, USA: Department of Mechanical Engineering, Stanford University, 1984.

Ong L., Wallace K. The velocity field of the turbulent very near wake of a circular cylinder // Experiments in Fluids. — 1996. — Vol. 20. — P. 441–453.

Parnaudeau P., Carlier J., Heitz D., Lamballais E. Experimental and numerical studies of the flow over a circular cylinder at Reynolds number 3900 // Physics of Fluids. — 2008. — Vol. 20, No. 8. — 085101.

Pope S. B. Turbulent flows. — Cambridge University Press, 2000. — 771 p.

Prandoni P., Vetterli M. Signal Processing for communications. — 1st edn. — New York: EPFL Press, 2008. — 300 p.

Rajani B. N., Kandasamy A., Majumdar S. LES of flow past circular cylinder at Re = 3900 // Journal of Applied Fluid Mechanics. — 2016. — Vol. 9, No. 3. — P. 1421–1435.

Rider W., Margolin L. The numerical analysis of implicit subgrid models // 16th AIAA Computational Fluid Dynamics Conference. — AIAA-2003-4101. — Orlando, Florida, 2003. — 11 p.

Ritos K., Kokkinakis I. W., Drikakis D. Performance of high-order implicit large eddy simulations // Computers & Fluids. — 2018. — Vol. 173. — P. 307–312.

Roshko A. Perspectives on bluff body aerodynamics // Journal of Wind Engineering and Industrial Aerodynamics. — 1993. — Vol. 49, No. 1–3. — P. 79–100.

Sieber M., Paschereit C. O., Oberleithner K. Spectral proper orthogonal decomposition // Journal of Fluid Mechanics. — 2016. — Vol. 792. — P. 798–828.

Snyder D. D., Degrez G. Large-eddy simulation with complex 2-D geometries using a parallel finite element/spectral algorithm // International Journal for Numerical Methods in Fluids. — 2003. — Vol. 41. — P. 1119–1135.

Stewart R. W., Townsend A. A. Similarity and self-preservation in isotropic turbulence // Philosophical Transactions of the Royal Society. — 1951. — Vol. 243. — P. 359–386.

Taylor G. The spectrum of turbulence // Proceedings of the Royal Society of London — Series A: Mathematical and Physical Sciences. — 1938. — Vol. 164 (919). — P. 476–490.

Tennekies H., Lumley J. L. A first course in turbulence. — M.I.T. Press, 1972. — 310 p.

Williamson C. H. K. Vortex dynamics in the cylinder wake // Annual review of fluid mechanics. — 1996. — Vol. 28. — P. 477–539.

Wissink J. G., Rodi W. Numerical study of the near wake of a circular cylinder // International Journal of Heat and Fluid Flow. — 2008. — Vol. 29, No. 4. — P. 1060–1070.